Applied Catalysis A, General 564 (2018) 123–132

Contents lists available at ScienceDirect

Applied Catalysis A, General

journal homepage: www.elsevier.com/locate/apcata

Facile encapsulation of P25 (TiO_2) in spherical silica with hierarchical porosity with enhanced photocatalytic properties for gas-phase propene oxidation

J. Fernández-Catalá, D. Cazorla-Amorós, Á. Berenguer-Murcia*

Materials Institute and Inorganic Chemistry Department, University of Alicante, Ap. 99, E-03080 Alicante, Spain

ARTICLE INFO

Keywords:
TiO_2
SiO_2
Composites
Photocatalytic activity
Propene

ABSTRACT

In this work, we have performed the encapsulation of a reference TiO_2 material (P25) in spherical silica with hierarchical porosity using a sol-gel methodology. The same P25 material has been encapsulated within a "classical" MCM-41 mesoporous silica and a precipitated silica. The materials synthesized in this work were characterized by ICP-OES, SEM, TEM, EDX, XRD, UV–VIS, TG, and nitrogen adsorption. It has been observed that the P25 samples encapsulated in silica present improved CO_2 production rates per mol of P25 in the photo-oxidation of propene, compared to P25 alone as well as the physical mixture of the two components. Moreover, the sample with a low content of P25 encapsulated in silica with hierarchical porosity presents the highest CO_2 production rates per mol of P25 with respect to the other P25/silica samples, due to a better accessibility of the titania phase and improved illumination of the active phase. Furthermore, the hierarchical porosity of the silica shell material favours mass transport and an increased concentration of reagents by adsorption near the titania phase. This improvement in photocatalytic activity is obtained by following a simple and reproducible synthesis methodology that employs an established silica preparation protocol. Thus, the choice of a silica with an adequate porosity for this application is proven to be a promising advancement in the development of efficient photocatalysts.

1. Introduction

One of the most extensively researched photocatalysts over the past decades up to date is titanium dioxide (TiO_2), due to its unique properties including high photocatalytic efficiency, physical and chemical stability, and relatively low cost and toxicity [1–3]. Moreover, this semiconductor is an important industrial product in many applications such as inorganic pigment, photocatalysis, sunscreen and energy storage, among others [4–10]. An interesting commercially available TiO_2 powder is P25 (EVONIK), which consists approximately of 80% anatase and 20% rutile titanium dioxide [11]. This commercial TiO_2 is widely used as photocatalyst in photochemical reactions due to its high activity both in aqueous phase and in gas phase [12]. In many cases P25 is used as benchmark material to compare the potential of different photocatalysts in both mediums [13,14].

Many factors influence the photocatalytic properties of TiO_2, such as particle size, morphology, exposed lattice planes, and crystalline phase [9,15,16]. Despite the fine-tuning through which P25 has already undergone, this material presents low surface area (it is essentially a non-porous material) and low concentration of active surface groups, such as hydroxyl groups, as main drawbacks [17].

In the last years, many efforts have been made to increase the porosity of TiO_2 by synthesis of new nanoporous TiO_2 materials [18–20]. Many works have also focused on the fabrication of Ti/Adsorbent composites or supported TiO_2 on the surface of adsorbents to improve the aforementioned factors, with the aim of enhancing the photocatalytic activity of TiO_2. The most interesting materials used as adsorbents in these composites are carbon materials, zeolites, mesoporous materials, and polymers, among others [17,21–23].

TiO_2/SiO_2 materials have attracted a great deal of attention due to the advantages of SiO_2 as support or as component of composites, due to its tunable surface area and pore size, as well as interconnectivity of the pore network facilitating mass transport, high surface acidity (presence of Ti-O-Si) species, abundant surface hydroxyl groups and transparency in a wide wavelength range in the UV/Vis region [17,24].

Some studies have pointed out that the photocatalytic activity of TiO_2/SiO_2 composites is worse than that of the pure TiO_2 due to a blocking effect exerted by the silica on the active phase. For example,

---

* Corresponding author.
E-mail address: a.berenguer@ua.es (Á. Berenguer-Murcia).

https://doi.org/10.1016/j.apcata.2018.07.024
Received 21 May 2018; Received in revised form 10 July 2018; Accepted 16 July 2018

K.J. Nakamura et al. showed a decreased rate of photocatalytic degradation of methylene blue when using TiO_2 encapsulated in SiO_2 [25]. Another report by M. Nussbaum et al. demonstrated that as the thickness of the SiO_2 shell (measured in SiO_2 layers prepared by chemisorption-oxidation cycles according to the authors) around the TiO_2 photocatalyst decreased the activity of the active phase [26].

On the other hand, many studies show that the presence of SiO_2 with TiO_2 particles is not deleterious. In fact, several reports point out that silica favours the photoactivity of TiO_2 [27–30]. In the last years, many efforts have been made to synthesize a nanostructured photocatalyst with enhanced adsorption and molecular-sieving properties, with tunable conformations, as well as improved mass transfer in order to optimize the activity of the photocatalyst. In this aspect, S. Wang et al. synthesised Core(TiO_2)@shell(SiO_2) nanoparticles, with a void interlayer [31]. Another approach was carried out by Y. Kuwahara et al. where they developed yolk–shell nanostructured photocatalysts, consisting of TiO_2 nanoparticles in the core of spherical hollow silica shells [32]. Also, X. Chen et al. synthesised TiO_2/SiO_2 and TiO_2/ZrO_2 nanocomposites with hierarchical macro/mesopores [29]. In all cases the authors intended the preparation of well-defined porous textures of their composites in order to favour mass transport and the selective concentration of reagents on the photoactive surface so as to optimize the photocatalytic activity. Some authors used this type of composites for the selective degradation of molecules due to the textural properties that silica brings forth to the composite [31,33].

Considering the extensive background, this work approach consists of a facile and reproducible synthesis of TiO_2/SiO_2 composites through the encapsulation of commercial P25 in silica materials with markedly different porous textures (combining micro, meso, and macro-porosity in the best case scenario) in order to improve the photocatalytic activity by enhancing the adsorption characteristics of the composites (see Scheme 1). In this respect, the use of a silica shell displaying hierarchical porosity favours the aspects commented previously. Also, this work studies the effect of the percentage of P25 encapsulated in the silica with hierarchical porous texture in order to test the illumination efficiency and optimize the photocatalytic activity. This type of study, has not been undertaken through this approach to the best of our knowledge.

The materials studied in this work will be tested in the elimination of propene since this type of composites (TiO_2/SiO_2) can improve the photooxidation of VOCs as reported in the literature [17,21]. Moreover, these compounds are known to be very harmful to the environment and human health [34,35]. In particular, this work deals with the removal of propene al low concentration because this molecule might be taken as a representative example of low molecular weight VOCs [36]. These results are compared to the benchmark P25 and other related materials [37,38], in order to study the effect of the porous texture of the silica on the photocatalytic performance.

2. Experimental section

2.1. Materials

Titanium Tetramethyl orthosilicate (TMOS, 99%, Sigma-Aldrich), Tetraethyl orthosilicate (TEOS, 99%, Sigma-Aldrich), glacial acetic acid (HAc, 99%, Sigma-Aldrich), Pluronic F-127 (F-127, Sigma-Aldrich), Cetyltrimethylammonium bromidedeionized (Sigma-Aldrich), urea (99%, Merck), ammonium hydroxide (NH_4OH, 30%, Panreac), absolute ethanol (EtOH, 99.8%, Fisher Scientific), TiO_2 (P25, Rutile: Anatase/ 85:15, 99.9%, 20 nm, Degussa) and deionized water were used in the present work. All reactants were used as received, without further purification. The ultrasonic probe equipment SONOPULS HD 2200 (BANDELIN electronic GmbH & Co. KG) was used to disperse the P25 powder in water.

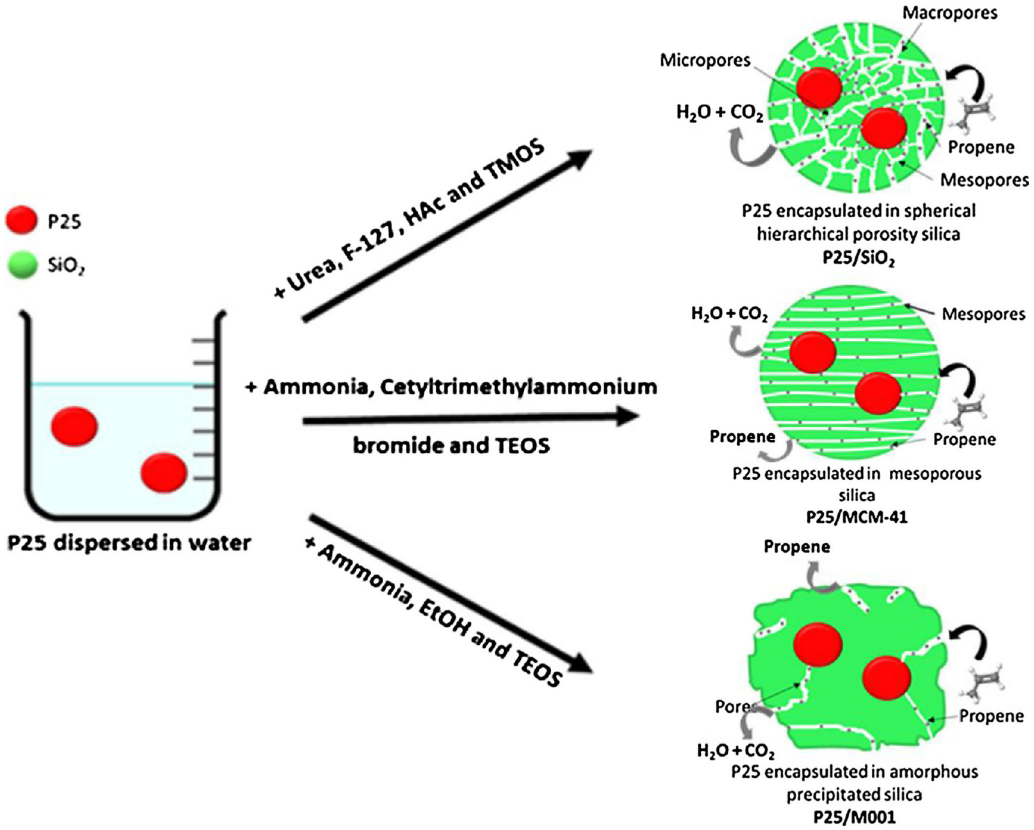

Scheme 1. Schematic representation of the synthetic procedure followed for the preparation of silica samples with different porous textures.

2.2. Preparation of P25 (TiO_2) encapsulated in silica with hierarchical porosity

Commercial TiO_2 (Evonik P25) was encapsulated in spherical silica with hierarchical porosity following a straightforward sol-gel synthesis adapted from previous reports [39].

As an illustrative example, the synthesis of the P25/spherical hierarchical silica done to obtain a nominal loading of 20 wt.% TiO_2 was performed as follows: 0.32 g of P25 were dispersed in 10.1 g of water using an ultrasound probe (Bandelin SONOPULS HD 2200) with a power of 660 W operating at 30% power for 5 min. In order to prepare the composite material, the P25 dispersion in water was mixed with 0.9 g of urea, 0.81 g of F-127 and 5.8 µl of glacial HAc. This solution was stirred for 80 min. The solution was cooled at 0 °C and 4 g of TMOS were added dropwise under vigorous stirring. The resulting solution was kept under stirring for 40 min at 0 °C. The solution was rapidly transferred to a 40 ml autoclave and heated at 40 °C for 20 h to promote gel formation. The temperature was later increased to 120 °C with a dwelling time of 6 h to promote the decomposition of urea to generate the mesoporosity. The resulting encapsulated P25 was calcined at 500 °C for 6 h with a heating rate of 1 °C/ min in order to remove the templates and any leftover reagents used in the synthesis.

In this work, the amount of P25 in the synthesis was changed to obtain composites with a nominal TiO_2 loading of 10 and 40 wt.% (0.16 g and 0.64 g, respectively). All samples were calcined as described above. The nomenclature of these samples is P25_10/SiO_2, P25_20/SiO_2 and P25_40/SiO_2 for the samples containing 10, 20, and 40 wt.% of nominal P25 loading, respectively.

2.3. Preparation of P25 (TiO_2) in a precipitated silica (M001) and a mesoporous silica (MCM-41)

For comparison purposes, two more composites of P25 encapsulated (20 wt.% nominal loading) with precipitated silica [37] and a mesoporous silica (MCM-41 type) [38] were also prepared. We used the same methodology as that employed to encapsulate the P25 in hierarchical silica.

The synthesis of the P25 encapsulated in a precipitated silica was performed as follows: 0.4 g of P25 were dispersed in 20 g of water with an ultrasound probe (Bandelin SONOPULS HD 2200) with a power of 660 W output operating at 30% power for 5 min. In order to prepare the composite material, the P25 dispersion in water was mixed with 4 ml of NH_4OH, 85 g of EtOH to favour the precipitation of the silica, 70 g of water and 8 ml of TEOS, at 380 rpm for 1 h. The mixture was filtered and dried overnight at 323 K. The resulting encapsulated P25 was calcined at 500 °C for 6 h with a heating rate of 1 °C/ min in order to remove the templates and any leftover reagents used in the synthesis. This sample was named P25/M001.

The synthesis of the P25 encapsulated in mesoporous silica was performed as follows: 0.4 g of P25 were dispersed in 20 g of water with an ultrasound probe (Bandelin SONOPULS HD 2200) with a power of 660 W operating at 30% power for 5 min. The composite material was prepared by dissolving 2 g of the templating agent (cetyltrimethylammonium bromide) in 76 g of deionized water. The mixture was stirred and heated gently until a clear solution was obtained. This mixture was added to the P25 dispersion in water, together with 4 ml of NH_4OH and 8 ml of TEOS. The resulting mixture was stirred at 380 rpm for 1 h. The suspension was filtered and dried overnight at 323 K. The resulting encapsulated P25 was calcined as described above. This sample was labelled as P25/MCM-41.

2.4. Samples characterization

The percentages of TiO_2 and SiO_2 present in the samples were analyzed by inductively coupled plasma emission spectroscopy (ICP-OES), in a Perkin-Elmer Optima 4300 system. Dissolution of the samples was carried out by treating them with HF at room temperature.

Thermogravimetric analysis was done in a thermobalance (SDT 2960 instrument, TA). In these analyses, the sample was heated up at 900 °C in air (heating rate of 5 °C min^{-1}).

X-ray diffraction (XRD) analysis was carried out in a SEIFERT 2002 equipment. Cu Kα (1.54 Å) radiation was used. The scanning velocity was 2°/min, and diffraction patterns were recorded in the angular 2θ range of 6–80 º.

The UV-VIS/DR spectroscopy analysis was performed in an UV–vis spectrophotometer (Jasco V-670), with an integrating sphere accessory and powder sample holder. $BaSO_4$ was used as the standard reference and the reflectance signal was calibrated with a Spectralon standard (Labsphere SRS-99-010, 99% reflectance). The absorption edge wavelength was estimated from the intercept at zero absorbance of the high slope portion of each individual spectrum in the range 200–800 nm (absorbance method). Then, the band gap can be calculated [40] as:

$$Eg = \frac{1239.8}{\lambda}$$

where Eg is the band gap energy (eV) and λ is the edge wavelength (nm).

Nitrogen adsorption–desorption isotherms were performed in an Autosorb-6B apparatus from Quantachrome [37]. Prior to analysis all samples were degassed at 250 °C for 4 h. BET surface area (S_{BET}) and total micropore volume (V_{N2}) were determined by applying the Brunauer–Emmett–Teller (BET) equation, and the Dubinin–Raduskevich equation to the N_2 adsorption data obtained at −196 °C, respectively. Total pore volumes were determined by nitrogen adsorption volume at a relative pressure of 0.95. Mesopore size distributions for all the samples were obtained applying the Barrett-Joyner-Halenda (BJH) equation to the N_2 desorption branch data from the adsorption isotherms at −196 °C, using the software provided by Quantachrome [41].

Transmission electron microscopy (TEM) images were taken using a JEOL JEM-2010 equipment. Field-emission scanning electron microscope (FE-SEM) images were taken using a ZEISS, Merlin VP Compact, this equipment has incorporated a microanalysis system by Energy Dispersive X-ray spectroscopy (EDX), BRUKER Quantax 400 for performing elemental mapping of Si and Ti species present in the samples.

2.5. Catalytic tests

The photocatalytic performance of the different materials was studied using an experimental system designed in our laboratory. The system consists of a vertical quartz reactor where the photocatalyst bed is placed on a quartz wool bed. The reactor is 50 mm in height, its diameter is 20 mm and the quartz wool support height is around 10 mm. A UV lamp is placed parallel to the quartz reactor, at a distance around 1 cm. The UV lamp radiation peak appears at 365 nm. The commercial reference of this lamp is TL 8 W/05 FAM (Philips, 1 W). Finally, the coupled quartz reactor lamp is surrounded by a cylinder covered with aluminum foil. A scheme of this system is depicted elsewhere [36].

The photocatalysts synthesised in this work were used for the oxidation of propene at 100 ppmv in air at room temperature under flow conditions. The calibrated gas cylinder was supplied by Carburos Metálicos, S.A.

The flow rate of the propene-containing stream was 30 (STP) ml/min after purging the reactor with helium.

The weight of photocatalyst used in these experiments was 0.11 g. However, in order to study the illumination efficiency and any possible inter-particle mass transfer issues, tests at different flow rates of propene were done in which the flow of propene and the mass of P25 were both changed in order to keep the space velocity constant (V_{sp} = flow (ml/min)/ mass of photocatalyst (g)) at a value of 257 ml/g·min. The ratio was 10 ml min^{-1}/0.0367 g, 20 ml min^{-1}/0.0735, 30 ml min^{-1}/0.11 g and 40 ml min^{-1}/0.147 g. This was done in order to properly compare the samples prepared in this study. In addition, the sample P25_40/SiO_2 was measured with the same V_{sp} (257 ml/g·min) with respect to the amount of P25. Additionally, blank tests were performed under the same experimental conditions as the catalytic tests but in absence of the photocatalysts, resulting in non detectable catalytic activity.

To better study the combined effect between the silica and the P25, the reactor was filled with both silica and P25 as separate powders in a configuration in which the silica with hierarchical porosity was either on top or under the titania. The resulting samples were named SiO_2/P25 and P25/SiO_2 respectively. Furthermore, a physical mixture of P25 and silica (containing the appropriate amount of P25) was also prepared with the same purpose, the nomenclature of this sample is PM.

The propene-containing stream was passed through the photocatalyst bed until the propene concentration was stable (after about 3 h). The lamp is then switched on and kept working until a constant propene signal is achieved, that is, steady state conditions (usually after 3 h) and, afterwards the outlet gas is continuously analyzed by mass spectrometry (Balzers, Thermostar GSD 301 01).

Propene conversion was calculated using the following expression:

$$\text{Propene conversion } (\%) = \frac{C_{\text{initial}_{C_3H_6}} - C_{\text{steady state}_{C_3H_6}}}{C_{\text{initial}_{C_3H_6}}} \times 100$$

where $C_{\text{initial } C3H6}$ is the initial propene concentration, 100 ppmv and $C_{\text{steady state}C3H6}$ is the propene concentration at steady state conditions in the outlet gas when the UV light is switched on. Moreover the CO_2 production rate was calculated per mol of P25, taken as the active phase, using the following expression (with the aim to normalize the results with the amount of P25):

$$CO_2 \text{ production rate } = \frac{q_{gen}}{n}$$

where q_{gen} is the molar flow rate of CO_2 generated (moles CO_2/s) and n is the moles of catalyst (moles of P25).

3. Results and discussion

3.1. P25/SiO_2 samples characterization

In this section, the results on the characterization for the P25 samples encapsulated in spherical silica with hierarchical porosity (SiO_2) are presented, emphasizing the effect of the P25 loading in the composites.

The results obtained by ICP-OES show the discrepancies between the nominal and real loadings analysed by ICP-OES in the samples (Table 1). The sample with 10 wt.% nominal loading of TiO_2, results in a 3.8 wt.% loading by ICP-OES analysis. The other samples encapsulated in hierarchical silica present the same trend as showed in Table 1. As a result of the analysis of ICP-OES, the samples P25_10/SiO_2, P25_20/SiO_2, P25_40/SiO_2 show a content of 3.8, 8.14 and 15.9 wt% of P25; these values will be used in the calculations in order to obtain reliable figures. The discrepancies between the nominal loading of TiO_2 and the results obtained for the ICP-OES technique may be due to a fraction of the P25 solid present in the dispersion which was not transferred to the reaction medium. In this aspect, we observed the presence of a significant amount of P25 solid adhered to the walls and in the bottom of the vessel where the dispersion was prepared after transferring this suspension.

Table 1
Percentage of titania of the sample prepared in this study.

Samples	% TiO_2 Nominal	% TiO_2 ICP-OES
P25_10/SiO_2	10	3.8 ± 0.9
P25_20/SiO_2	20	8.1 ± 0.2
P25_40/SiO_2	40	15.9 ± 0.3

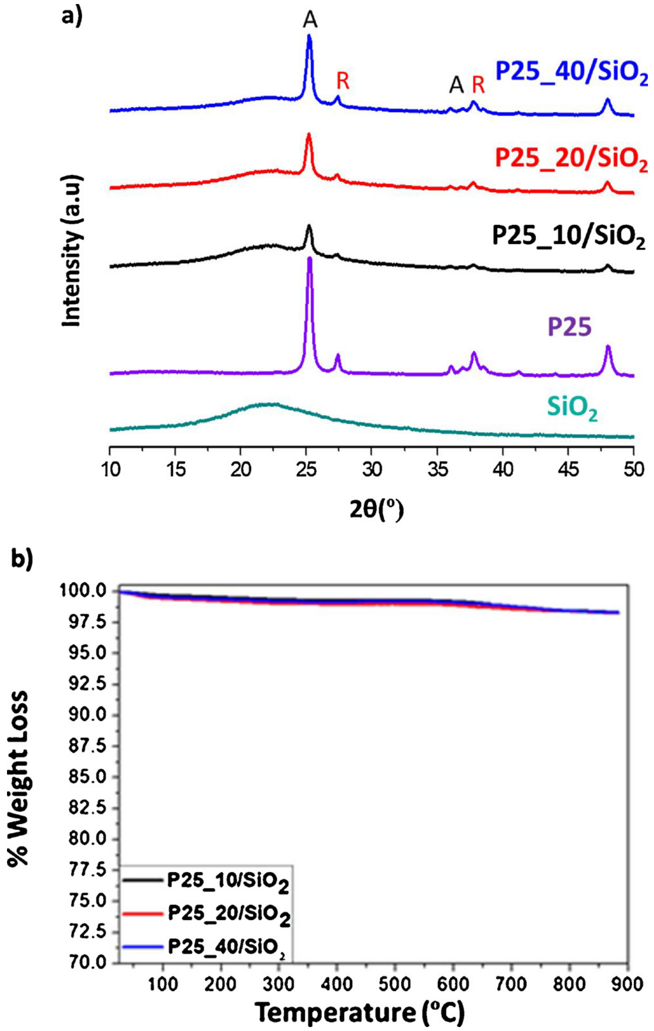

Fig. 1. (a) XRD patterns of all composites prepared with hierarchical porosity silica. The data for the SiO_2 and P25 are showed for comparison. Key: A = anatase; R = rutile (b) TG curves of the P25 encapsulated with hierarchical porosity silica.

The XRD pattern of the P25/SiO_2 samples with different P25 loading are showed in Fig. 1(a). In all cases, the particles of P25 encapsulated in silica have the same crystalline phases as the benchmark P25 (rutile and anatase) after calcination at 500 °C, indicating the presence of P25 in all composites (P25_10/SiO_2, P25_20/SiO_2 and P25_40/SiO_2) without any further modification. An elbow in the XRD pattern of all composites due to the presence of amorphous silica is also observed, as showed in the pattern for the naked SiO_2 sample [39]. TG analyses show a small weight loss of approximately 2 wt% in all samples (see Fig. 1(b)). This suggests that all organic matter and any leftover reagents present in the synthesis were eliminated in the calcination step. The low weight percentage losses observed might be due to adsorbed water or the possible decomposition reactions of hydroxyl groups at higher temperatures [16].

The UV–vis spectra obtained for the P25/SiO_2 with different P25 loading samples are showed in Fig. 2. All hybrid photocatalysts with different loading of P25 show a similar absorption band edge at 400 nm. This fact indicated that the loading of P25 in the composite does not modify the absorption range and the band gap of the P25. However the composites show a small discrepancy in the absorbance range and in the band gap with respect to the naked P25 (Fig. 2)

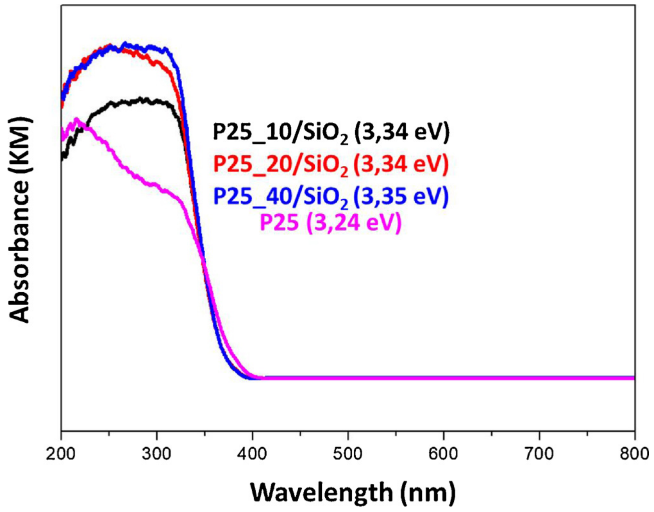

Fig. 2. UV-VIS absorption spectra and band gap value (Eg) of the P25/SiO$_2$ with different P25 loading samples. The data for the benchmark material P25 are showed for comparison.

indicating that the presence of the silica can slightly modify the band gap of P25 from 3.2 to 3.3 eV.

The porous texture of the synthesized samples was investigated by N$_2$ adsorption measurements as showed in Fig. 3. The N$_2$ physisorption isotherm of P25 shows a typical type-II isotherm, indicative of a non-porous solid. However, the sample does present a hysteresis in the high relative pressure range due to interparticle adsorbate condensation. The SiO$_2$ prepared in our research group is a combination of type I and IV isotherms, typical of mesoporous materials with a certain degree of microporosity. This silica has hierarchical porosity, presenting micro, meso and macro-porosity [39]. As expected, the composites obtained in this work present similar isotherms to that of the pure hierarchical SiO$_2$ material, with a noticeable decrease in the adsorption uptake at low relative pressures and the hysteresis loop as the P25 loading increases.

Concerning the textural properties showed in Table 2, the BET surface area and V$_{total}$ 0.95 decreases with increasing P25 loading, as commented in the previous paragraph. However, the textural parameters cannot help in distinguishing whether the P25 is encapsulated or not in the SiO$_2$. Comparing the S$_{BET}$ (obtained from the isotherms) and T_S$_{BET}$ (obtained theoretically assuming that the composite is a physical mixture), the samples with lower quantities of P25 (P25_10/SiO$_2$ and P25_20/SiO$_2$) show a discrepancy of only 7% between S$_{BET}$ and T_S$_{BET}$. Nevertheless, the samples with the highest loading of P25 (P25_40/SiO$_2$) shows a much higher discrepancy (45%) between S$_{BET}$ and T_S$_{BET}$. This difference indicates that high TiO$_2$ loadings severely affect the final morphology of the obtained composite, resulting not only in a modification of the porous texture, but also in the shaping of the final SiO$_2$/TiO$_2$ sample (vide infra). In this sense, it appears that high concentrations of suspended TiO$_2$ powder prevents the spinodal decomposition of the SiO$_2$-rich phase, resulting in a composite with an irregular morphology. As a result, the mixing law fails to apply for this sample.

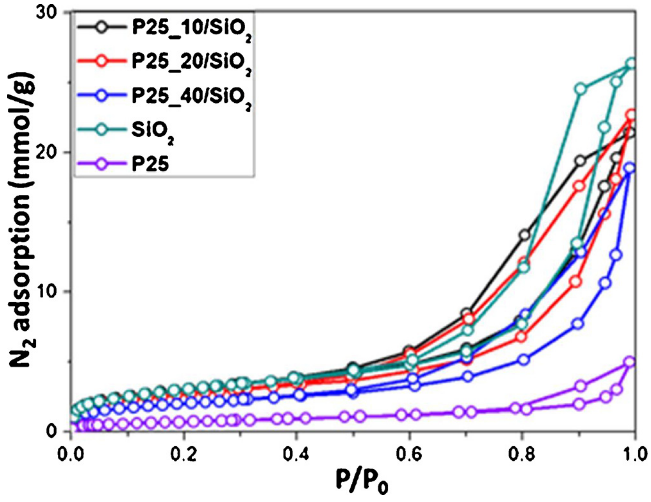

Fig. 3. N$_2$ isotherms at 77 K for the different composites with hierarchical porosity silica samples. The adsorption isotherm of SiO$_2$ and P25 is also show for comparison purposes.

Table 2
Textural properties of the samples prepared in this study. The data for SiO$_2$ and P25 are showed for comparison purposes.

Samples	S$_{BET}$ (m^2/g)	T_S$_{BET}$* (m^2/g)	V$_{total,0.95}$ (cm^3/g)	V$_{N2DR}$ (cm^3/g)	Mean pore size (nm)
SiO$_2$	244	–	0.86	0.10	6.2
P25_10/SiO$_2$	235	252	0.61	0.10	7.9
P25_20/SiO$_2$	215	230	0.57	0.09	7.9
P25_40/SiO$_2$	145	219	0.38	0.07	6.2
P25	54	–	0.18	0.02	7.6

* T_S$_{BET}$ represents the theoretical S$_{BET}$ of the composites synthesised in this work (considering the composites as a physical mixture). This value was calculated by the following expression: T_S$_{BET}$ = (S$_{BET}$ (Mesoporous silica) · (SiO$_2$ present in the composites (ICP-ES)) + (S$_{BET}$ (P25) · P25 present in the composites (ICP-ES)).

TEM images are showed in Fig. 4. The TiO$_2$ crystals are encased in the hierarchical silica matrix (Fig. 4(a)). Moreover, the SiO$_2$ is clearly surrounding the P25 particles in the sample P25_20/SiO$_2$, which corroborates the encapsulation of the TiO$_2$ inside the SiO$_2$ matrix. Fig. 4b shows the presence of P25 in the sample P25_20/SiO$_2$ as the particle shows the lattice fringes and interplanar distances characteristic of both anatase and rutile present in P25 particles.

SEM images show that the samples with low P25 loadings (3.8% and 8.14 wt.%) (Fig. 5(a) and (b)) have a spherical morphology typical for this silica (Fig. 5(d)) [39]. No particles with irregular morphology (representative of P25 NPs, Fig. 5(e)) are observed for these samples, which indicates the encapsulation of P25 inside the SiO$_2$ matrix, as already hinted at by the TEM images. However the sample with the highest P25 loading (P25_40/SiO$_2$) presents both spherical and irregular particles (Fig. 5(c)), in agreement with the comments made from the adsorption isotherms results.

EDX mapping images are presented in Fig. 6(a)–(c). Sample P25_10/SiO$_2$ contains Ti in the composites indicating that P25 is probably inside the SiO$_2$ shell, owing to the composite presenting a spherical structure as observed in the SEM images (Fig. 6(a)). This is a clear indication that the spinodal decomposition process is not largely affected by the presence of the TiO$_2$ powder. For sample P25_20/SiO$_2$ a similar observation can be made although the presence of Ti is more noticeable as showed in Fig. 6(b), allowing us to conclude that in both composites the P25 particles are encapsulated within the SiO$_2$ matrix. Nevertheless, the sample with the highest TiO$_2$ loading (sample P25_40/SiO$_2$, Fig. 6(c)), presents a morphology distinct from spherical, which shows that the spinodal decomposition is modified in the presence of large concentrations of photocatalyst. In turn, this encapsulated TiO$_2$ sample shows a significantly different morphology from the other two samples as corroborated by the SEM images and the textural parameters of these composites, in which the mixing law does not apply. In order to better compare the results towards an understanding of the encapsulation phenomenon Fig. 7(a) and (b) show EDX images mapping of sample P25_20/SiO$_2$ and a physical mixture in which the two phases are clearly and completely separated, with no observable encapsulation.

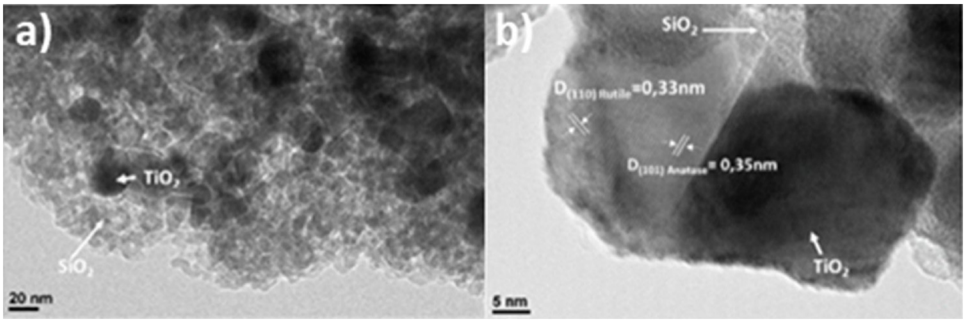

Fig. 4. TEM images of a representative sample prepared in this study: (a) P25_20/SiO$_2$, (b) Magnification of P25 NPs (sample P25_20/SiO$_2$).

3.2. P25/M001 and P25/MCM-41 samples characterization

In this section, the results on the characterization of the P25 samples encapsulated inside precipitated silica (M001) and a mesoporous silica (MCM-41) with a nominal TiO$_2$ content of 20% are discussed. These results are compared with P25 encapsulated in spherical hierarchical silica (P25_20/SiO$_2$) to better put the results in perspective.

The results obtained by ICP-OES (Table 3) show discrepancies between the samples encapsulated in different silicas where all samples have a 20 wt.% nominal of P25. The sample with P25/M001 presents the lowest TiO$_2$ loading (3.2 wt.%). The other samples P25/MCM-41 and P25_20/SiO$_2$ present a similar TiO$_2$ loading, 6.8 wt.% and 8.1 wt.%, respectively, being the sample with the P25 encapsulated in hierarchical silica the one with the highest loading. These values will be used in the calculations in order to obtain reliable figures.

The XRD pattern for the P25 encapsulated in different silica samples (M001, MCM-41 and SiO$_2$) are showed in Fig. 8. The particles of P25 encapsulated in the different silicas present the same crystalline phases as the benchmark P25 (rutile and anatase) after calcination at 500 °C, indicating the presence of P25 in the composites without any further modification as indicated previously in Fig. 1 (a) for the composite (P25_20/SiO$_2$). In these composites with different silicas (P25/M001, P25/MCM-41 and P25/SiO$_2$) an elbow in each of the XRD patterns was also observed, indicating the presence of the different silicas (M001, MCM-41 and SiO$_2$) in each composite used in this study.

The UV–vis spectra obtained for the P25 encapsulated with different silica (M001, MCM-41 and SiO$_2$) are showed in Fig. 9. All hybrid photocatalysts with different silica samples present a similar absorption band edge at 400 nm and band gap. These values indicate that the use of different silica (M001, MCM-41 and SiO$_2$) does not modify the light absorption of the P25 encapsulated.

The N$_2$ adsorption measurements at 77 K are showed in Fig. 10. The N$_2$ physisorption isotherm of sample M001 shows a type-II isotherm, indicative of a non-porous material, with some porosity arising from a small hysteresis in the high relative pressure range due to interparticle condensation. However, the composite P25/M001 presents a combination of type I and type IV isotherms. This fact is remarkable since this composite with P25 (non-porous material) has higher N$_2$ adsorption capacity with respect to the naked M001, indicating the appearance of additional porosity when the composite is formed probably due to interparticle spacings with sizes in the below-nanometer region. The silica MCM-41 shows a combination of types I and IV isotherms, typical of mesoporous materials with a certain degree of microporosity as it has been reported in the literature [37]. As expected, the composites obtained with this silica present similar isotherms to that of the pure MCM-41, with a noticeable decrease in the adsorption uptake at low pressures and the hysteresis loop due the presence of a non-porous material (P25).

The textural properties obtained from the adsorption isotherms are showed in Table 4. The BET surface area and V$_{total}$ 0.95 decrease with the incorporation of P25 except in the case of the P25/M001 sample where these values increase. The samples with MCM-41 present the highest surface area and total pore volume.

TEM images show the possible encapsulation of P25 inside the different silicas. (Fig. 11). SEM images show the morphology of the samples P25/M001, P25/MCM-41 and P25_20/SiO$_2$ (Fig. 12(a–c)). The samples P25/M001 and P25/MCM-41 present an irregular morphology, a feature common for both precipitated silica and P25. EDX mapping images are presented in Fig. 12(d)–(f). All samples present Ti in the composites indicating that P25 is inside the different silicas as observed

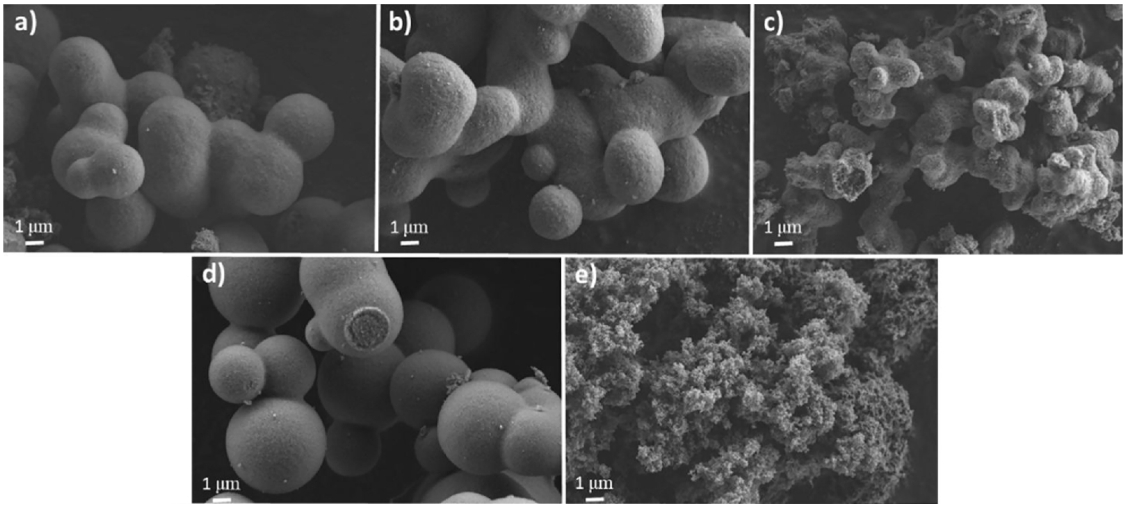

Fig. 5. SEM of the samples with hierarchical porosity silica: (a) P25_10/SiO$_2$, (b) P25_20/SiO$_2$, (c) P25_40/SiO$_2$. The SEM images of SiO$_2$ (d) and P25 (e) are also showed for comparison purposes.

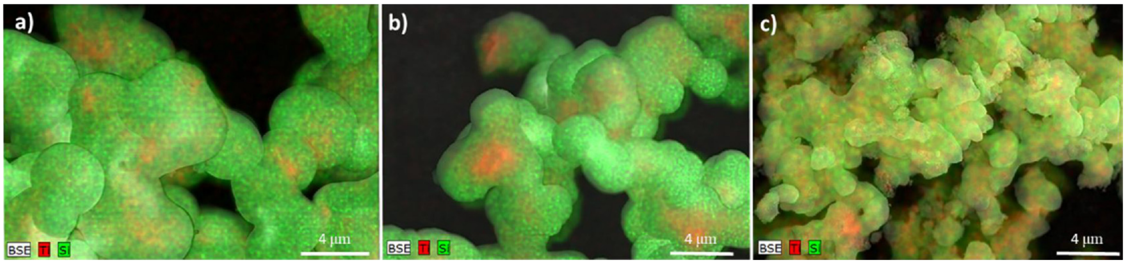

Fig. 6. EDX images mapping of the samples (a) P25_10/SiO_2, (b) P25_20/SiO_2, (c) P25_40/SiO_2.

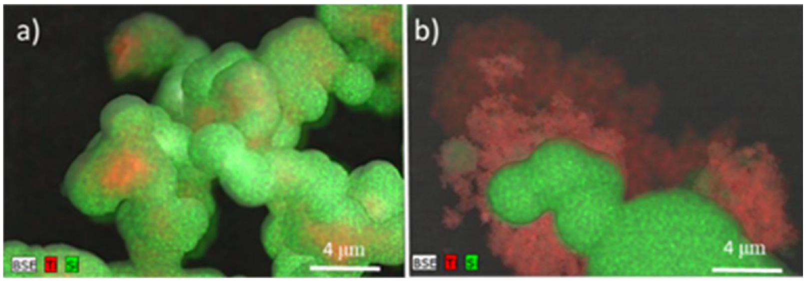

Fig. 7. EDX images mapping of the composite and the physical mixture with the same percentage of P25 (a) P25_20/SiO_2 (composite), (b) PM (Physical mixture).

Table 3
Percentage of titania of the sample with different silica samples.

Samples	% TiO_2 ICP-OES
P25/M001	3.2 ± 0.1
P25/MCM41	6.8 ± 0.9
P25_20/SiO_2	8.1 ± 0.2

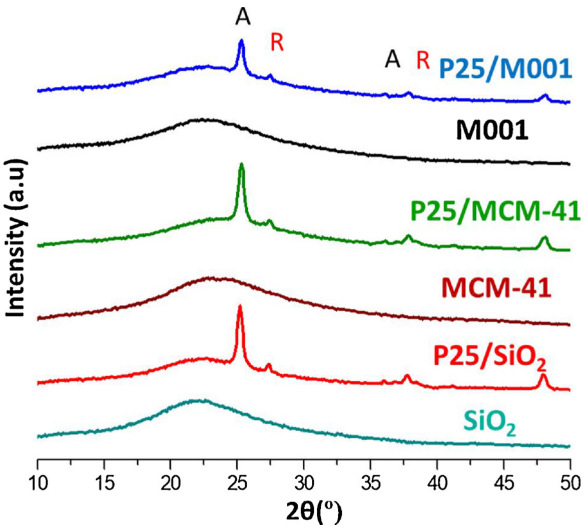

Fig. 8. XRD patterns of the composites with different silica. The data for the different silica used in this work are showed for comparison Key: A = anatase; R = rutile.

for sample P25_20/SiO_2.

3.3. Photocatalytic activity

The photocatalytic activity of the materials prepared in this work was evaluated by studying the mineralization of propene in the gas phase at low concentration (100 ppmv in air) to CO_2 at room temperature, following the global reaction showed in Eq. (1) [36].

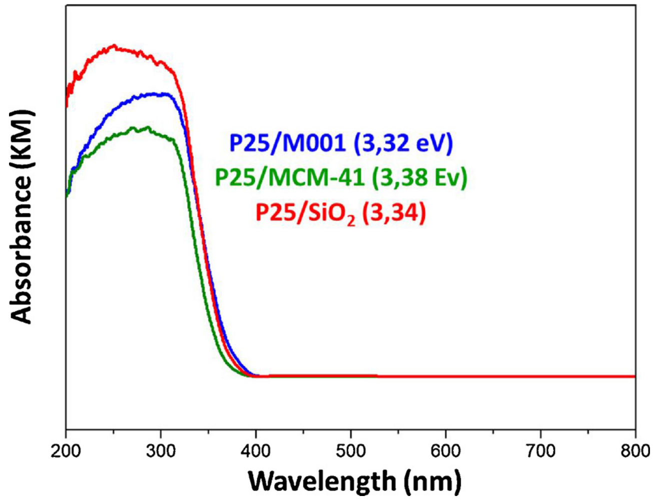

Fig. 9. UV-VIS absorption spectra and the band gap (Eg) of the P25/SiO_2 with different silica samples.

$$2C_3H_6 + 9O_2 \leftrightarrow 6CO_2 + 6H_2O \quad (1)$$

It must be noted that in this study the mechanism of total photooxidation of VOCs was not studied since it has been extensively studied and reported in the literature [36,42]. Given that the samples used in this study do not differ significantly from those studies, it is safe to assume that the mechanism should be identical to that previously reported.

The results of the effect of different P25 loadings in the photocatalytic activity of the samples with the hierarchically porosity silica are showed in Fig. 13 (a). The naked P25 presents the best value of propene conversion with respect to the composites where the P25 was encapsulated in the spherical hierarchical silica (SiO_2). In the case of the composites, as the concentration of P25 (active phase) is increased propene conversion increases. Nevertheless the samples with 8.1 wt.% and 15.9 wt.% P25 loading present approximately the same propene conversion. This might be due to sample P25_40/SiO_2 presenting a different morphology with respect to the other composites and this factor affects the activity of the composite (Fig. 13(a)). When the results

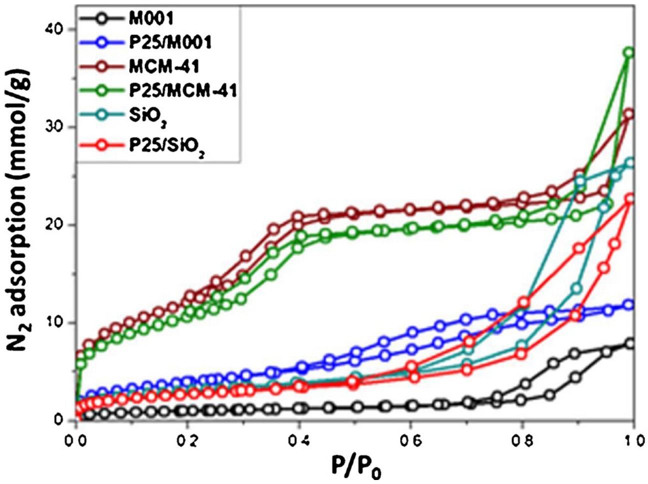

Fig. 10. N_2 isotherms at 77 K for the samples prepared in this study: P25/M001, P25/MCM-41, and P25_20/SiO_2. The adsorption isotherms of the pure silicas are also showed for comparison purposes.

Table 4
Textural properties of the samples prepared in this study derived from the analysis of the N_2 adsorption isotherms. The data for SiO_2 and P25 are showed for comparison purposes.

Samples	S_{BET} (m^2/g)	$V_{total,0.95}$ (cm^3/g)	V_{N2DR} (cm^3/g)	Mean pore size (nm)
M001	77	0.25	0.033	6.2
MCM-41	973	0.82	0.39	2.9
SiO_2	244	0.86	0.10	6.2
P25/M001	317	0.39	0.17	3.1
P25/MCM-41	875	0.77	0.34	3.1
P25_20/SiO_2	215	0.57	0.09	7.9
P25	54	0.18	0.02	7.6

of the photocatalytic activity are normalized per mol of active phase (P25) (CO_2 production rate) expressed as moles CO_2/(moles P25 X s), P25 has the lowest photoactivity compared to the composites due to the silica favouring the activity per mol of P25 as showed in the literature [24]. With respect to CO_2 production rate, the composites show a decrease in the conversion of propene upon increasing the percentage of P25 in the composite which might be due to the change in porous texture and morphology of the silica or to another important factor such as the better illumination efficiency [43] of particles of P25 when the composites have lower percentages of active phase as explained later. Moreover in this section we evaluated the durability of the samples in specific the P25_10/SiO_2 as reference sample. The conditions used in this test have been described in the Catalytic Test section but running the propene abatement tests continuously for 14 h. In this sample the propene conversion was stable after 14 h of reaction (the initial and final propene conversion values were kept at 14%). In this sense, this sample (P25_10/SiO_2) was also recycled three times. For this purpose the sample was cycled in the photooxidation of propene as described in the Catalytic Test for three cycles (the conversion values for the three consecutive cycles was 14%). The performance of the sample did not show a noticeable change in the propene conversion value at the end of each cycle.

In order to deepen into the synergy between silica and P25 upon encapsulation in these materials as described in literature [21,23,29], the sample showing the highest TiO_2 loading (P25_40/SiO_2), is compared in propene mineralization with composites in different configurations (PM, SiO_2/P25 and P25/SiO_2) as described in the Catalytic Tests section. As showed above (Fig. 13(b)), the naked P25 presents the best propene conversion value with respect to the other samples, due to the composites having a significantly lower amount of P25. In the composites and the mixtures (SiO_2 and TiO_2), the sample with the P25 encapsulated has better propene conversion than the other samples. This result indicates a synergetic effect between the encapsulated P25 and the SiO_2; it seems that hierarchical silica favours mass transport and increases the concentration of reagents near the P25 particles.

Interestingly, P25 has the lowest photocatalytic activity when expressed as rate of CO_2 formation per moles of P25, compared to the composites (Fig. 13(b)) even when the P25 sample is not encapsulated. In the case of the composites, the encapsulation of P25 (Fig. 13(a)) improved the activity per mol of P25. This is observed in the conversion of propene for the P25_xx/SiO_2 samples, which hints at a synergy between the P25 encapsulated inside the hierarchical silica. In this respect, the coexistence of a hierarchical porosity which favours mass transfer of reagents and products, the possibility of this same porosity acting as an adsorbent for reagents, and the intimate contact between the SiO_2 and TiO_2 phase results in an improved performance of the encapsulated samples compared with all its physically mixed counterparts (Fig. 13(b)).

From our results showed in Table 2 and Fig. 14, it would appear that there is a correlation between the BET surface area in the composites and their CO_2 production rate in the propene mineralization reaction. With this in mind, from the values showed in Table 4, the TiO_2 sample encapsulated in MCM-41 (SiO_2) should outperform all samples. This material should better concentrate the reagents favouring their oxidation by the TiO_2 phase, as explained in the literature [21,25,29]. In order to probe into this effect in the activity of encapsulated P25, the CO_2 production rates for the samples with silica having different textural parameters (S_{BET}) and morphologies are showed in Fig. 14. Interestingly, the composite with hierarchical silica presents the highest CO_2 production rate, despite having poorer textural parameters. It is also observed that the sample encapsulated in mesoporous silica shows better photooxidation of propene than that in microporous silica. This result evidences the importance of using a silica not only with large surface area but also with hierarchical porosity for optimizing the mass transport in addition to an increased concentration of reagents due to the hierarchical porosity interconnected which allows all the adsorbed propene to arrive at the active phase (P25) even comparing these samples with others showing a BET surface area four times larger which lack this hierarchical structure as showed in Scheme 1. In the MCM-41 sample, the porous structure (tubular non-interconnected mesopores)

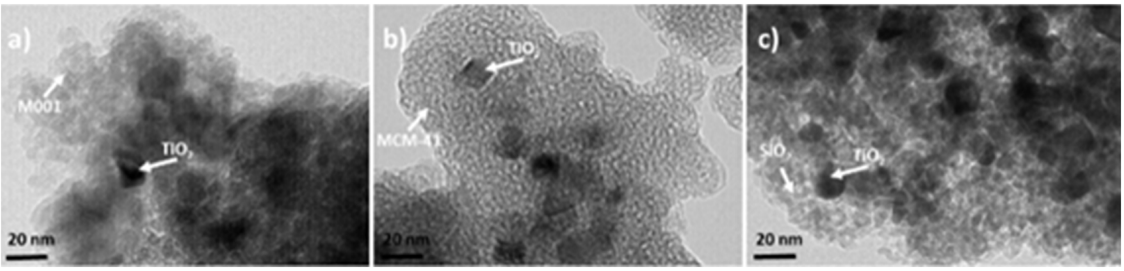

Fig. 11. TEM of the composite prepared in this study: (a) P25/M001, (b) P25/MCM-41, (c) P25_20/SiO_2.

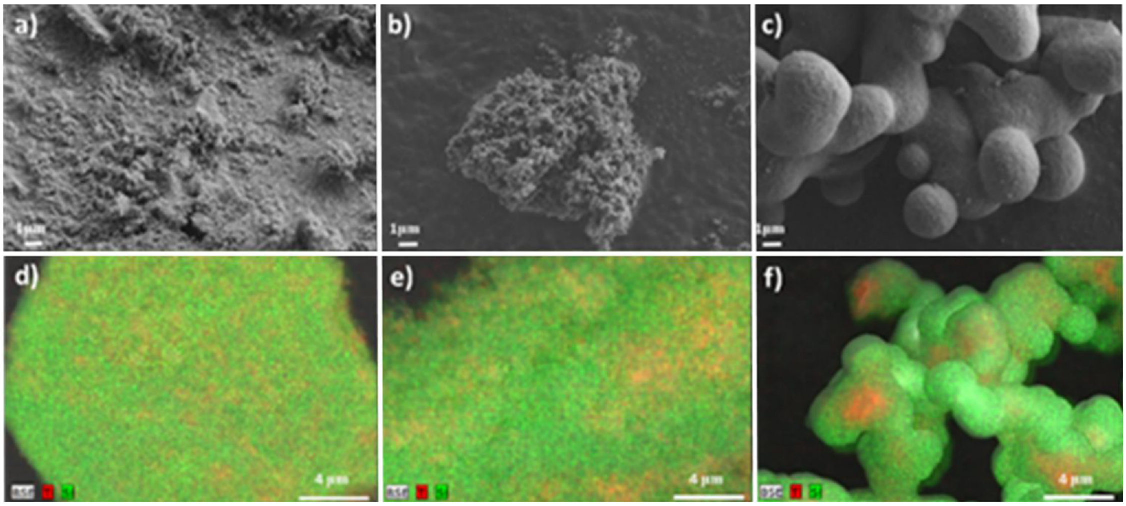

Fig. 12. SEM of the samples with different silica: (a) P25/M001, (b) P25/MCM-41, (c) P25_20/SiO_2. Fig. 12(d–f) present the EDX images mapping (d) P25/M001, (e) P25_20/MCM-41, (f) P25_20/SiO_2.

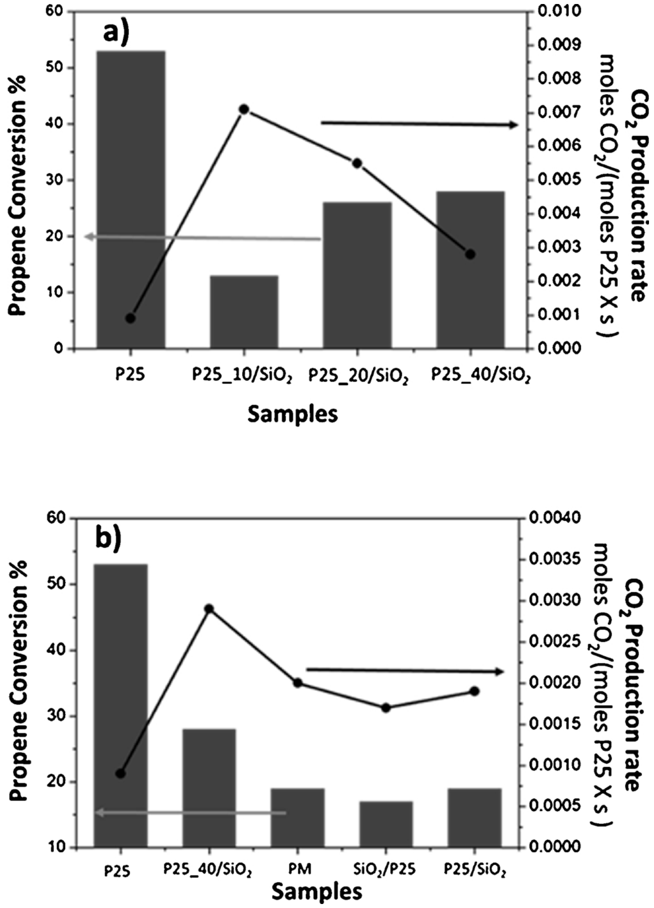

Fig. 13. Comparison of propene conversion and CO_2 production rates for samples with spherical hierarchical porosity silica and P25 for comparison purposes: (a) Photoxidation varying the percentage of P25 in the samples, (b) Comparison of the composite P25_40/SiO_2 with samples where the same amount of P25 is not encapsulated.

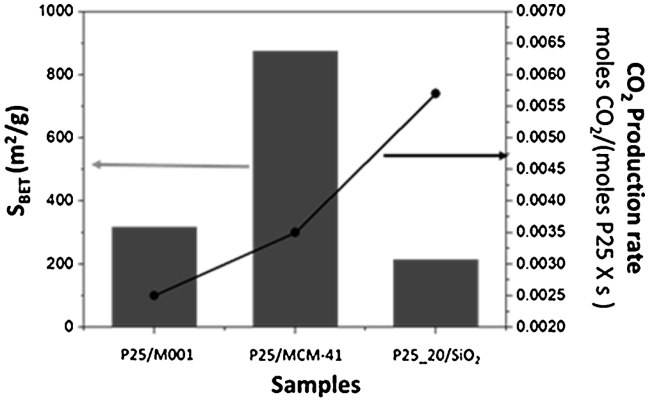

Fig. 14. Comparison of CO_2 production rates of samples of P25 encapsulated in different silica and its textural parameters (S_{BET}).

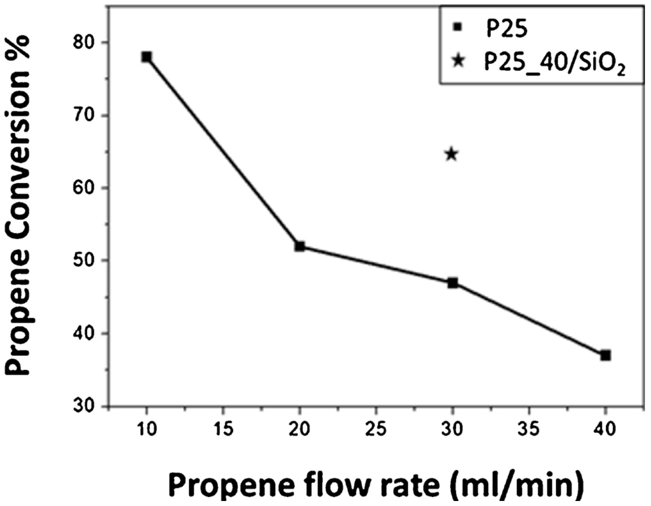

Fig. 15. Comparison of propene conversion with different flow rates (The mass of the samples is described in Experimental section) maintaining a constant space velocity of 257 ml·g^{-1} min^{-1} (See Experimental section). The sample P25_40/SiO_2 with the same mass of P25 (0.11 g) and space velocity is included for comparison purposes.

does not guarantee a good access to the active phase via the mesopores, since many of them may not be connected with the P25 particles. On the other hand, in the silica with hierarchical porosity (SiO_2) the interconnected porosity allows a much higher accessibility to the active sites, favouring the oxidation of propene on P25, as showed in Scheme 1.

With the purpose of studying the possible effect of the better illumination efficiency in the encapsulated P25 particles as discussed before, the conversion of propene was also obtained by varying the propene flow and the mass of P25 (Fig. 15) keeping the space velocity (V_{sp}) constant with the purpose of comparing the naked P25 samples with different mass as described in the Catalytic Test section. These catalytic tests are usually done to detect diffusional limitations. The results show an increase in propene conversion as the flow of reagents and mass of catalysts are decreased. This is markedly different from the expected results for classic catalysis, where the conversion remains constant until it decreases due to diffusional problems [44]. This result indicates some contribution of the photonic efficiency [43]. When the weight of the sample (in this case only P25) is decreased (and consequently the particles bed size), the propene conversion increases due to a better illumination of the particles. This factor could partially explain the increased photocatalytic activity of the composites compared to P25 as showed in Fig. 13(b). In fact, the results of the comparison of the samples P25 (0.11 g of naked P25) and P25_40/SiO_2 (0.69 g of composite), which represents the worst case scenario in illumination efficiency for the encapsulated P25 particles, performed at the same V_{sp} with respect to the amount of P25 (adding in both cases 0.11 g of P25 in the reactor), indicate a double effect: one arising from the better illumination of the TiO_2 particles because the P25 particles are kept within a UV-transparent shell in the composite; this effect combines with the presence of hierarchical porosity that enhances the conversion of propene as showed Fig. 14. These results indicated the difficulty in separating the significant effect brought forth by the porosity of the silica shell (as showed in Fig. 14) and the contribution of the improved illumination efficiency in the photocatalyst (as showed in Fig. 15).

Considering the results obtained in this study in terms of characterization of samples and their performance in the photocatalytic oxidation of propene at low concentrations, the most promising outlook seems to be the following: (1) this work presents a facile encapsulation of P25 in different SiO_2 materials through a simple and reproducible sol-gel method, providing a synergetic effect between the P25 and the silica; (2) the increase in TiO_2 loading decreases the activity of the P25/SiO_2 samples, due to the change in the morphology of the composites (TiO_2_40/SiO_2) and the importance of the illumination efficiency of the active phase; (3) the synergetic effect between the silica and P25 takes place upon encapsulation due to an intimate contact of the P25 with the silica which acts as adsorbent for the propene molecules and this favours photoactivity; (4) The election of a suitable (i.e. interconnected) porous texture of the silica matrix allows the improved photoactivity of the photocatalyst per mol of P25.

With the results discussed above, the encapsulation of P25 (TiO_2) in spherical silica with hierarchical porosity, which can be prepared by a simple, reproducible, and cost-effective sol-gel method displays a remarkable photocatalytic activity with respect to the benchmark P25 and the P25 encapsulated in a standard precipitated silica (M001) or mesoporous silica (MCM41). This approach opens the door to synthetic encapsulation strategies [25] with high performance in photoactivity of elimination of VOCs at low concentration using an adequate silica without using convoluted or advanced synthesis methods [32,45].

4. Conclusions

In this study, a facile encapsulation of P25 (TiO_2) in different silica materials (spherical silica with hierarchical porosity, mesoporous silica and precipitated silica) was performed from a modification of an established methodology. The sample P25_10/SiO_2 presents the best improvement of CO_2 production rate per mol of P25, because the increase in the loading of P25 causes a modification in the morphology and porosity of the composite and a diminished illumination efficiency affecting photocatalytic activity. Apart from the synergetic effect between the silica and P25, encapsulation provides and added bonus due to an intimate contact of the P25 with the silica what favours photoactivity. Another important factor is the election of a correct porous network for the silica matrix. This fact, allows to synthesize new materials with an improved mass transfer and catalytic efficiency for the abatement of contaminants at low concentrations in gas phase.

Acknowledgements

The authors thank MINECO (Project CTQ2015-66080-R, MINECO/FEDER) for financial support. JFC thanks MINECO for a researcher formation grant (BES-2016-078079).

References

[1] J. Winkler, Titanium Dioxide: Production, Properties and Effective Usage, 2nd ed., Vincentz Network, Germany, 2013.
[2] G. Liu, J.C. Yu, G.Q. Lu, H.M. Cheng, Chem. Commun. 47 (2011) 6763–6783.
[3] J. Schneider, M. Matsuoka, M. Takeuchi, J. Zhang, Y. Horiuchi, M. Anpo, D.W. Bahnemann, Chem. Rev. 114 (2014) 9919–9986.
[4] X. Chen, S.S. Mao, Chem. Rev. 107 (2007) 2891–2959.
[5] D. Dionysiou, G.L. Puma, J. Ye, J.D. Schneider, W. Bahnemann, Photocatalysis: Applications, Royal Society of Chemistry, Cambridge, 2016.
[6] A. Mills, S.K. Lee, J. Photochem. Photobiol. A Chem. 152 (2002) 233–247.
[7] A. Fujishima, K. Honda, Nature 238 (1972) 37–38.
[8] M. Grätzel, Nature 414 (2001) 338–344.
[9] M. Ouzzine, M.A. Lillo-Ródenas, A. Linares-Solano, Appl. Catal. B Environ. 134 (2013) 333–343.
[10] R. Daghrir, P. Drogui, D. Robert, Ind. Eng. Chem. Res. 52 (2013) 3581–3599.
[11] B. Ohtani, O.O. Prieto-Mahaney, D. Li, R. Abe, J. Photochem. Photobiol. A Chem. 216 (2010) 179–182.
[12] J. Ryu, W. Choi, Environ. Sci. Technol. 42 (2008) 294–300.
[13] J. Coronado, F. Fresno, M.D. Hernández-Alonso, R. Portela, Design of Advanced Photocatalytic Materials for Energy and Environmental, 1st ed., Springer, 2013 pag.88.
[14] E. Lichtfouse, J. Schwarzbauer, D. Robert, Green Materials for Energy, Products and Depollution, 1st ed., Springer, 2013 pag.77.
[15] M. Yasmina, K. Mourad, S.H. Mohammed, C. Khaoula, Energy Procedia 50 (2014) 559–566.
[16] L. Cano-Casanova, A. Amorós-Pérez, M. Ouzzine, M.A. Lillo-Ródenas, M.C. Román-Martínez, Appl. Catal. B Environ. 220 (2018) 645–653.
[17] X. Qian, K. Fuku, Y. Kuwahara, T. Kamegawa, K. Mori, H. Yamashita, ChemSusChem 7 (2014) 1528–1536.
[18] D.M. Antonelli, J.Y. Ying, Angew. Chemie Int. 34 (1995) 2014–2017.
[19] H. Hou, M. Shang, L. Wang, W. Li, B. Tang, W. Yang, Sci. Rep. 5 (2015) 1–9.
[20] J. Fernández-Catalá, L. Cano-Casanova, M.A. Lillo-Ródenas, A. Berenguer-Murcia, D. Cazorla-Amorós, Molecules 22 (2017) 2243–2259.
[21] Y. Paz, Solid State Phenom. 162 (2010) 135–162.
[22] R. Leary, A. Westwood, Carbon 49 (2011) 741–772.
[23] Y. Kuwahara, H. Yamashita, J. Mater. Chem. 21 (2011) 2407–2416.
[24] C. Anderson, A.J. Bard, J. Phys. Chem. 99 (1995) 9882–9885.
[25] K.J. Nakamura, Y. Ide, M. Ogawa, Mater. Lett. 65 (2011) 24–26.
[26] M. Nussbaum, Y. Paz, Phys. Chem. Chem. Phys. 14 (2012) 3392.
[27] K. Tanabe, J. Catal. 231 (1974) 225–231.
[28] A. Corma, M.T. Navarro, J.P. Pariente, J. Chem. Soc. Chem. Commun. (1994) 147–148.
[29] X. Chen, X. Wang, X. Fu, Energy Environ. Sci. 2 (2009) 872.
[30] H. Yoshida, C. Murata, T. Hattori, Chem. Commun. (1999) 1551–1552.
[31] S. Wang, T. Wang, W. Chen, T. Hori, Chem. Commun. (2008) 3756–3758.
[32] Y. Kuwahara, Y. Sumida, K. Fujiwara, H. Yamashita, ChemCatChem 8 (2016) 2781–2788.
[33] P. Nadrah, M. Gaberšček, A.S. Škapin, Appl. Surf. Sci. 405 (2017) 389–394.
[34] H.J. Rafson, Odor, VOC Control Handbook, 1st ed., McGraw Hill, USA, 1998.
[35] S.E. Manahan, Environmental Chemistry, 8th ed., CRC Press, USA, 2004.
[36] M.A. Lillo-Ródenas, N. Bouazza, A. Berenguer-Murcia, J.J. Linares-Salinas, P. Soto, A. Linares-Solano, Appl. Catal. B Environ. 71 (2007) 298–309.
[37] A. Berenguer-Murcia, D. Cazorla-Amorós, Á. Linares-Solano, Adsorp. Sci. Technol. 29 (2011) 443–455.
[38] A. Berenguer-Murcia, A.J. Fletcher, J. García-Martínez, D. Cazorla-Amorós, A. Linares-Solano, K.M. Thomas, J. Phys. Chem. B 107 (2003) 1012–1020.
[39] J. García-Aguilar, I. Miguel-García, Berenguer-Murcia, D. Cazorla-Amorós, ACS Appl. Mater. Interfaces 6 (2014) 22506–22518.
[40] A.R. Gandhe, J.B. Fernandes, J. Solid State Chem. 178 (2005) 2953–2957.
[41] M. Thommes, K. Kaneko, A.V. Neimark, J.P. Olivier, F. Rodriguez-Reinoso, J. Rouquerol, K.S.W. Sing, Pure Appl. Chem. 87 (2015) 1051–1069.
[42] Y. Huang, S.S.H. Ho, Y. Lu, R. Niu, L. Xu, J. Cao, S. Lee, Molecules 21 (2016) 359–389.
[43] J.M. Herrmann, J. Photochem. Photobiol. A Chem. 216 (2010) 85–93.
[44] H.S. Fogler, Elements of Chemical Reaction Engineering, Prentice Hall, USA, 2006.
[45] S. Ikeda, Y. Ikoma, H. Kobayashi, T. Harada, T. Torimoto, B. Ohtani, M. Matsumura, Chem. Commun. (2007) 3753–3755.